



# Effects of neodymium substitution on the structural, optical, and magnetic properties of yttrium iron garnet nanoparticles

Marwa H. El Makdah<sup>1</sup> · Mohammad H. El-Dakdouki<sup>1</sup> · Rami Mhanna<sup>2</sup> · Jamal Al Boukhari<sup>3</sup> · Ramadan Awad<sup>3</sup>

Received: 18 January 2021 / Accepted: 24 March 2021 / Published online: 2 April 2021  
© The Author(s), under exclusive licence to Springer-Verlag GmbH, DE part of Springer Nature 2021

## Abstract

Neodymium ( $\text{Nd}^{3+}$ )-doped yttrium iron Garnet (YIG) nanoparticles, with compositional variation of  $\text{Nd}_x\text{Y}_{3-x}\text{Fe}_5\text{O}_{12}$  ( $0.0 \leq x \leq 3.0$ ), were prepared by co-precipitation method. The prepared nanoparticles were characterized using TGA, XRD, TEM, SEM, EDX, and FTIR. The calcination temperature was chosen according to the maximum decomposition temperature ( $\sim 810^\circ\text{C}$ ) achieved in TGA. XRD confirmed the successful phase formation, at the chosen sintering temperature ( $1100^\circ\text{C}$ ), of Garnet for  $x < 3.0$  (cubic  $Ia\bar{3}d$  symmetry), after which the orthoferrite phase  $\text{NdFeO}_3$  at  $x = 3.0$  (orthorhombic  $Pnma$  symmetry) was formed. The incorporation of  $\text{Nd}^{3+}$  increased the lattice parameters ( $12.3833\text{--}12.5020 \text{ \AA}$ ), porosity ( $34.127\text{--}39.549\%$ ) and crystallite size ( $82.66\text{--}129.99 \text{ nm}$ ). Agglomerated, distorted, and irregularly shaped nanoparticles were observed in TEM and SEM with the elemental composition confirmed by EDX, inconsistency with the proposed  $\text{Nd}_x\text{Y}_{3-x}\text{Fe}_5\text{O}_{12}$ . The FTIR analysis revealed the characteristic bands at  $657$ ,  $600$ , and  $565 \text{ cm}^{-1}$  with  $\text{Nd}^{3+}$  doping concentration between  $0.0$  and  $1.5$ . These bands disappeared at  $x = 3.0$ , where the orthoferrite phase of  $\text{NdFeO}_3$  dominated. UV–Vis spectroscopy revealed the semiconducting behavior of the prepared samples with energy gaps ranging between  $2.89$  and  $3.02 \text{ eV}$ . A broad emission band was observed, in the range  $500\text{--}550 \text{ nm}$ , in the PL spectra of all the prepared samples in agreement with the calculated band energies. The transport properties were studied by DC conductivity measurements and analyzed by the Arrhenius plots, from which two activation energies were determined for each sample. The magnetic properties, investigated by VSM, showed that isovalent substitution of  $\text{Y}^{3+}$  by  $\text{Nd}^{3+}$  dramatically influenced room temperature parameters, such as saturation magnetization, coercivity, and remanence magnetization.

**Keywords**  $\text{Nd}_x\text{Y}_{3-x}\text{Fe}_5\text{O}_{12}$  · Coprecipitation · Photoluminescence · Saturation magnetization

## 1 Introduction

Yttrium iron Garnet ( $\text{Y}_3\text{Fe}_5\text{O}_{12}$ ; YIG) is an important ferromagnetic material characterized by its notable thermal stability, magnetic, electric, and magneto-optical properties [1]. YIG is constantly being assessed as a supreme microwave material to improve the performance of microwave devices due to its low microwave loss [2]. YIG is also used

as a microwave absorber for minimizing electromagnetic interference at the high GHz frequency region [3]. Recently, YIG has attracted attention in the areas of spintronics and magnonics [4]. It belongs to the space group  $O_h^{10}\text{--}I_a\bar{3}d$ , with overall cubic symmetry, consisted of eight formula units and three sub-lattices [5]. One sub-lattice is occupied by  $\text{Y}^{3+}$  ions in dodecahedral sites 24(c), while the tetrahedral 24(d) and octahedral(16a) sites are occupied by  $\text{Fe}^{3+}$  ions, leading to outstanding-exchange interactions between the magnetic ions in the several sub-lattices [5, 6].

Aiming to understand and control the intrinsic properties of Garnet, such as the specific magnetization and coercivity, several studies reported the effect of substituting trivalent yttrium cations by different rare earth elements with the same electronic charge, such as  $\text{Ce}^{3+}$ ,  $\text{Dy}^{3+}$ ,  $\text{Gd}^{3+}$ ,  $\text{Sm}^{3+}$ ,  $\text{La}^{3+}$ ,  $\text{Nd}^{3+}$  and  $\text{Pr}^{3+}$  [7, 8]. In particular, the  $\text{Nd}^{3+}$  ion received special attention due to its unique magneto-optical properties [9]. It has been reported that substituting

✉ Marwa H. El Makdah  
sama\_mak@hotmail.com

<sup>1</sup> Department of Chemistry, Faculty of Science, Beirut Arab University, Beirut, Lebanon

<sup>2</sup> Department of Biomedical Engineering, Faculty of Engineering, American University of Beirut, Beirut, Lebanon

<sup>3</sup> Department of Physics, Faculty of Science, Beirut Arab University, Beirut, Lebanon

$\text{Nd}^{3+}$  in YIG improves their magneto-optical properties [10], bandwidth efficiency [11], dielectric properties, and magnetization values [12]. Enhancing magnetization values increases the Curie temperature ( $T_c$ ), and thus minimizes the potential variations in the magnetic properties of the Garnet with temperature [12]. Besides, doping YIG with rare-earth ions such as  $\text{La}^{3+}$ ,  $\text{Nd}^{3+}$ , and  $\text{Ce}^{3+}$  enhances the Gilbert damping parameter ( $\alpha$ ) and reduces the relaxation time, rendering the lanthanide-doped YIG a good candidate for broad-band-width microwave filters, higher-band 5G technology, and design of high-speed memory devices [13].

Several synthetic procedures were developed for the preparation of pure YIG, such as sol–gel [14], ball milling [15], hydrothermal [16], microwave heating [17], co-precipitation [18], and solid state [18]. The chemical, microstructure, and physical properties of the synthesized Garnets are affected by the method of preparation [18]. The co-precipitation method remains the most commonly used one, due to its reproducibility, low cost, aqueous reaction milieu, and high product yield and purity [18].

As the quest towards improving the magnetic and electric properties of YIG continues to attract attention from the industrial and technological sectors, we aim in the current study to investigate the effect of substituting the magnetic rare-earth cation  $\text{Nd}^{3+}$  in YIG lattice on the structural, optical, electrical, and magnetic properties of the doped materials. Several  $\text{Nd}_x\text{Y}_{3-x}\text{Fe}_5\text{O}_{12}$  nanoparticles with different compositions ( $0.0 \leq x \leq 3.0$ ) were synthesized using the simple and cost-effective co-precipitation method. The systematic characterization of the prepared nanoparticles reveals their phase content, chemical composition, and morphology, in correlation with their optical, electrical, and magnetic properties.

## 2 Experimental techniques

### 2.1 Materials

The precursors that were used to synthesize the  $\text{Nd}_x\text{Y}_{3-x}\text{Fe}_5\text{O}_{12}$  nanoparticles, by the coprecipitation method, include iron (III) chloride hexahydrate ( $\text{FeCl}_3 \cdot 6\text{H}_2\text{O}$ , [99%]), obtained from Fluka, neodymium (III) chloride hexahydrate ( $\text{NdCl}_3 \cdot \text{H}_2\text{O}$ , [99.9%]), purchased from Sigma Aldrich, yttrium (III) chloride ( $\text{YCl}_3$ , [99.99%]), purchased from Alfa Aesar, and sodium hydroxide, purchased from Alpha Chemika. Also, the deionized water was used as the dispersing solvent throughout the coprecipitation method. The drying and the annealing stages were performed by using an oven (Trade Raypa) and a Nabertherm box furnace, respectively.

### 2.2 Preparation of $\text{Nd}_x\text{Y}_{3-x}\text{Fe}_5\text{O}_{12}$ nanoparticles

The synthesis of the  $\text{Nd}_x\text{Y}_{3-x}\text{Fe}_5\text{O}_{12}$  nanoparticles, via the coprecipitation method, was initialized by reacting the appropriate amounts of  $\text{NdCl}_3 \cdot 6\text{H}_2\text{O}$ ,  $\text{FeCl}_3 \cdot 6\text{H}_2\text{O}$ , and  $\text{YCl}_3$ . The starting materials were dissolved in 100 mL of deionized water, and the reaction mixture was magnetically stirred for 1 h at room temperature. The mixture was titrated with 3 M NaOH to reach  $\text{pH} = 12$ , as monitored by a pH-meter, and then heated for 4 h at  $80^\circ\text{C}$  to precipitate the solution. The nanoparticles were collected by suction filtration and washed with deionized water till the mother liquor had a  $\text{pH} = 7$ . The samples were dried in an oven at  $100^\circ\text{C}$  for 18 h. Thereafter, the dried powders were grinded and annealed at  $1100^\circ\text{C}$  for  $x = 0.0$  (YIG) and  $1050^\circ\text{C}$  for  $0.0 < x \leq 3.0$  ( $\text{Nd}_x\text{Y}_{3-x}\text{Fe}_5\text{O}_{12}$ ) for 2 h to obtain the desired nanoparticles.

### 2.3 Characterization of $\text{Nd}_x\text{Y}_{3-x}\text{Fe}_5\text{O}_{12}$ nanoparticles

Thermogravimetric analysis (TGA) was carried out with a Bruker TGA-IR Tensor 27 NETZSCH TG 209 F1 LIBRA in an  $\text{N}_2$  atmosphere. The prepared nanoparticles were placed in a  $100\ \mu\text{L}$   $\text{Al}_2\text{O}_3$  crucible and heated from  $30$  to  $1100^\circ\text{C}$  with a heating rate of  $10^\circ\text{C}\ \text{min}^{-1}$ . The lattice parameters and crystallite size of the prepared samples were determined using X-ray diffraction (XRD) (Model: D8 FOCUS BRUKER), employing  $\text{Cu-}k_\alpha$  radiation ( $k_\alpha = 0.154\ \text{nm}$ ) in the range  $5^\circ \leq 2\theta \leq 80^\circ$ . Transmission electron microscopy (TEM) micrographs were collected on a Transmission Electron Microscope (JEOL 1400 plus) operated at  $80\ \text{kV}$ . The microstructure morphology and grain size of the nanoparticles were shown using AIS 2300 Cryo-Scanning Electron Microscopy (CSEM), operated at  $20.0\ \text{kV} \times 3.0\ \text{K}$ , with a resolution power of  $10\ \mu\text{m}$ . The atomic percentage of nanoparticles was measured using Energy-Dispersive X-ray analysis (EDX) detector-type SDD Apollo X at an accelerating voltage of  $20\ \text{kV}$ . Fourier Transform Infrared (FTIR) spectra of the nanoparticles were obtained on an FTIR Nicolet iS5 in the range  $400\text{--}1000\ \text{cm}^{-1}$ . Ultraviolet–visible spectroscopy (UV–Vis) absorption spectra for the nanoparticles were recorded using a JASCO V-670 spectrophotometer in the range of  $250\text{--}700\ \text{nm}$ . Photoluminescence (PL) was deliberated using a JASCO spectrofluorometer FP-8600 in the range  $500\text{--}700\ \text{nm}$ . DC conductivity was carried out with the two-probe method in the temperature range of  $373.15\text{--}873.15\ \text{K}$ , where the resistance was recorded in steps of  $10\ \text{K}$  during the sample cooling. Room temperature magnetic hysteresis (M–H) was performed using a vibrating sample magnetometer (VSM) (Lake Shore7410),

in the field range  $-20$  to  $20$  k Oe, to study the magnetic properties of the prepared samples.

## 3 Results and discussion

### 3.1 Thermogravimetric analysis (TGA)

The thermal stability of the  $\text{Nd}_x\text{Y}_{3-x}\text{Fe}_5\text{O}_{12}$  nanoparticles was addressed by investigating its decomposition performance using TGA under nitrogen atmosphere where samples were heated in the temperature range from  $30$  to  $1100$  °C. The effect of calcination temperature on the crystalline structures of the materials was extracted from the simultaneous TG–DTA curves shown in Fig. 1. An overall weight loss of 21.3%, 21.4%, 24.7% and 19.3% was observed for  $x=0.0$ , 0.5, 1.5 and 3.0, respectively. The endotherm observed between  $75$  and  $150$  °C corresponded to the loss of residual moisture [18]. Decomposition started at  $190$  °C and thermal stability was achieved at  $\sim 810$  °C with no further thermal decomposition thereafter. The weight loss observed over a wide temperature range from  $150$  to about  $810$  °C can be ascribed to the decomposition of amorphous precipitates into oxides [19]. The broad exothermic peak observed in the temperature range  $500$ – $700$  °C is associated

with crystallization of amorphous  $\text{YFeO}_3$ , and the exotherm occurring at the temperature range of  $800$ – $1100$  °C corresponded to the formation and crystallization of YIG [18, 20]. Accordingly, the calcination temperature was chosen to be between  $1050$  and  $1100$  °C, which is higher than the obtained final decomposition temperature to assure the total decomposition of the preparation precursors and complete crystallization of YIG.

### 3.2 X-ray diffraction patterns

The XRD patterns of the prepared  $\text{Nd}_x\text{Y}_{3-x}\text{Fe}_5\text{O}_{12}$  nanoparticles, depicted in Fig. 2a, mainly illustrate the Garnet phase with complete crystallization, occurring at the selected temperature. For undoped YIG ( $x=0.0$ ), the complete phase of pure YIG was achieved at  $1100$  °C, showing peaks with the hkl planes (400), (420), (422), (521), (532), (444), (640), (642), (800), (840), (842) and (664), which can be attributed to planes of a cubic unit cell [11]. The proper Garnet structure peaks (400), (420), and (422) are resolved, confirming that the prepared YIG Garnet belongs to the space group  $Ia\bar{3}d$  with a cubic crystal structure [21]. The existence of the Garnet phase for YIG nanoparticles is observed from the structure peak (420) [22]. The single Garnet phase of YIG is satisfactorily formed at  $1100$  °C with a lattice parameter

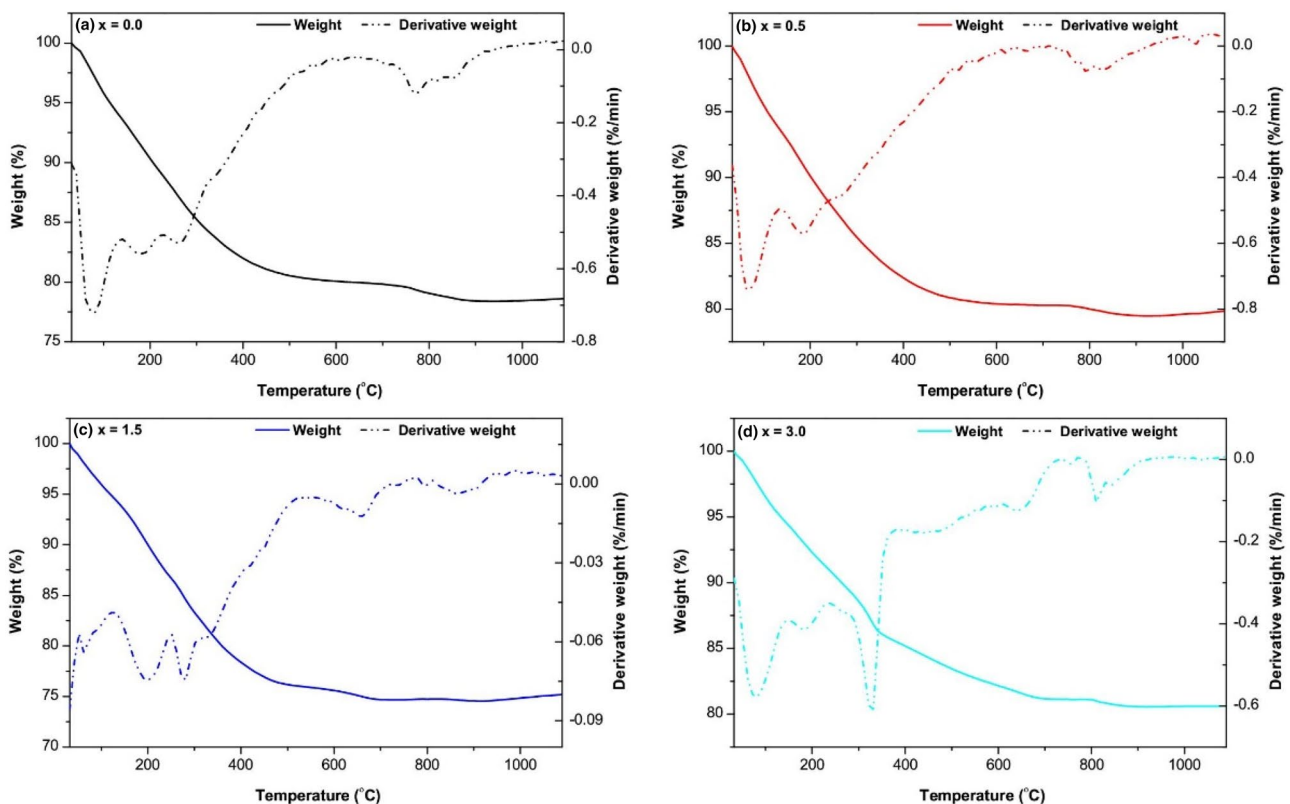
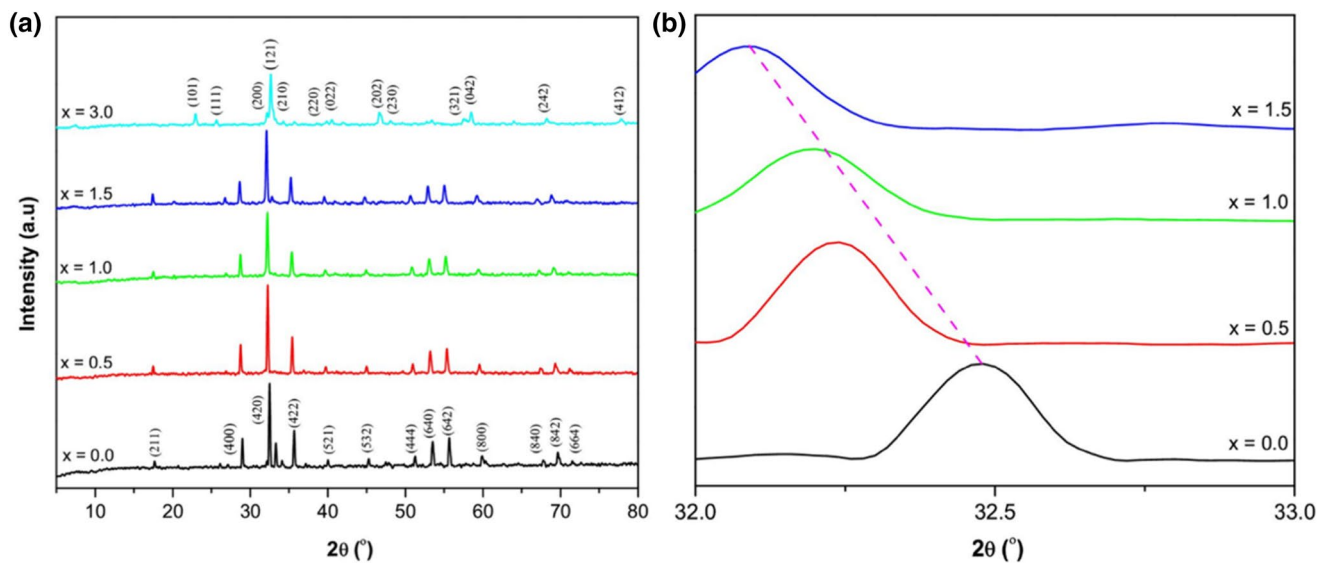


Fig. 1 TGA graphs of  $\text{Nd}_x\text{Y}_{3-x}\text{Fe}_5\text{O}_{12}$  nanoparticles synthesized by co-precipitation method at different Nd-doping concentrations



**Fig. 2** **a** XRD patterns for  $\text{Nd}_x\text{Y}_{3-x}\text{Fe}_5\text{O}_{12}$  nanoparticles and **b** peak shifting in (420) crystal plane due to  $\text{Nd}^{3+}$  doping

**Table 1** The phase contents of the synthesized nanoparticles and the reliability factors as determined by the MAUD program

	$x$				
	0.0	0.5	1.0	1.5	3.0
Phase (wt.%)					
$\text{Y}_3\text{Fe}_5\text{O}_{12}$	77.327	96.255	95.297	94.042	–
$\text{Nd}_3\text{Fe}_5\text{O}_{12}$	–	0.313	–	–	0.024
$\text{YFeO}_3$	21.866	2.747	2.413	2.286	–
$\text{NdFeO}_3$	–	–	1.441	3.672	82.891
$\alpha\text{-Fe}_2\text{O}_3$	0.807	0.685	0.849	–	17.084
$\chi^2$	1.44	1.26	1.27	1.36	1.36
$R_{\text{wp}}$	3.377	3.352	3.617	3.862	4.428
$R_{\text{exp}}$	2.341	2.653	2.839	2.834	3.264

of 12.3865 Å without any further reflections [23]. The XRD spectra of the  $\text{Nd}^{3+}$ -doped YIG nanoparticles ( $x=0.5, 1.0,$  or 1.5) revealed peak shifting of (420) crystal plane to lower

$2\theta$  as shown in Fig. 2b [13].  $\text{Y}^{3+}$  ions occupying the dodecahedral c-site in YIG crystal lattice were partially replaced by the doped  $\text{Nd}^{3+}$  ions, leading to an increase in the lattice parameter ' $a$ ' (Table 2). This observation is in uniformity with multiple literature reports [12, 13, 22, 24]. The Garnet phase is noticed mainly in samples having  $x=0.0, 0.5, 1.0,$  and 1.5. On the other hand, the orthoferrite ( $\text{NdFeO}_3$ ) phase is dominant in the case of  $x=3.0$  in addition to more phases, thus proving that a higher concentration of  $\text{Nd}^{3+}$  inhibits the crystallization of the Garnet phase [25]. XRD analysis showed that the  $\text{NdFeO}_3$  nanoparticles were excellently crystallized in the orthorhombic system, with the main peak at (121) planes [26]. Other peaks related to  $\text{Fe}_2\text{O}_3$  and NdIG were observed (Table 1). This  $\text{NdFeO}_3$  structure is categorized in the orthorhombic  $Pnma$  phase [26], with lattice constants  $a, b,$  and  $c,$  listed in Table 2.

The influence of strain on peak broadening was examined using the Williamson–Hall (W–H) method, where an individual contribution to line broadening  $\beta$  at full width at

**Table 2** Structural parameters of  $\text{Nd}_x\text{Y}_{3-x}\text{Fe}_5\text{O}_{12}$  nanoparticles obtained from XRD and TEM results

$x$	$2\theta$ (°)	Lattice parameter (Å)	$\rho_{\text{X-ray}}$ (g/cm <sup>3</sup> )	$\rho_{\text{bulk}}$ (g/cm <sup>3</sup> )	$P$ (%)	$\varepsilon$ ( $\times 10^{-3}$ )	$D_{\text{XRD}}$ (nm)	$D_{\text{TEM}}$ (nm)	$I_{\text{cry}}$	
0.0	32.29	$a$	12.3883	5.166	3.403	34.127	0.8	57.77	82.66	1.430
0.5	32.21		12.4165	5.319	3.387	36.323	1.5	86.66	92.45	1.066
1.0	32.08		12.4649	5.447	3.503	35.689	1.7	69.33	74.99	1.081
1.5	31.70		12.5020	5.585	3.596	35.613	1.8	72.98	77.64	1.063
3.0	32.49	$a$	5.5878	6.961	4.208	39.549	2.9	115.55	129.99	1.124
		$b$	7.7702							
		$c$	5.4567							

half maximum (FWHM) of Bragg reflection was expressed as follows [27]:

$$\beta = \beta_D + \beta_\epsilon, \quad (1)$$

where  $\beta_D$  is due to the contribution of crystallite size and  $\beta_\epsilon$  is due to strain-induced broadening.

$$\beta \cos \theta = \frac{k\lambda}{D} + 4\epsilon \sin \theta, \quad (2)$$

where  $k$  is the shape factor and is usually taken 0.89 for spherical crystallites with a cubic unit cell [28].

Equation (2) represents the modified W–H formula and addresses the uniform deformation model (UDM), where the strain is assumed uniform in all crystallographic directions. The strain and the average crystallite size can be determined from the slope and the intercept of the plot of  $\beta \cos \theta$  as a function of  $4 \sin \theta$ , respectively, as shown in Fig. 3f. The positive slope value indicates the tensile strain. The scattered data in Fig. 3f showed that the crystallite size and strain do not vary monotonically according to the W–H formula for different samples. This suggests that the broadening of the Bragg diffraction peaks for the different Bragg reflections is caused by an anisotropic microstrain. The extracted values from W–H plots are summarized in Table 2.

The % porosity ( $P$ ) of the synthesized samples was calculated according to [29]:

$$\%P = \left(1 - \frac{\rho_{\text{bulk}}}{\rho_{\text{x-ray}}}\right) \times 100 \quad (3)$$

where  $\rho_{\text{x-ray}}$  and  $\rho_{\text{bulk}}$  are the X-ray density and the bulk density ( $\rho_{\text{bulk}}$ ), respectively, given by the following relations [30, 31]:

$$\rho_{\text{X-ray}} = \frac{nM}{N_A V} \quad (4)$$

$$\rho_{\text{bulk}} = \frac{m}{\pi r^2 h} \quad (5)$$

where  $n$  is the number of atoms per unit cell, (8 is for the cubic  $Ia-3d$  structure and 4 is for the orthorhombic structure),  $M$  is the molecular weight,  $N_A$  is Avogadro's number,  $V$  is the unit cell volume, ( $a^3$  in the cubic  $Ia-3d$  structure and  $abc$  for the orthorhombic structure),  $m$  is the mass of the pressed pellets,  $r$  is the pellet's radius, and  $h$  is its thickness.

Upon Nd-doping, the porosity of the samples increases. Several factors affect the % porosity of a sample such as intergranular porosity, intragranular porosity, and grain size. The change in bulk density and porosity might be attributed to the greater atomic mass and radius of  $\text{Nd}^{3+}$  ions compared to iron (55.85 a.m.u). Assessing the average grain size, porosity, and degree of agglomerations of Nd-doped YIG

nanoparticles is essential for Garnet ferrite commercialization [30].

### 3.3 Microstructural analysis

The morphology and particle size of the synthesized nanoparticles was inspected by TEM, and the collected images are portrayed in Fig. 4. The TEM images display distinguishable, distorted, and irregularly shaped nanoparticles. It can be noticed that the addition of the  $\text{Nd}^{3+}$  ions did not alter the overall morphology of the prepared nanoparticles, although it caused a change in the particle size. The particle size distributions of the prepared nanoparticles are shown in the histograms of Fig. 4, constructed using ImageJ software. The values of the mean particle size ( $D_{\text{TEM}}$ ) for the  $\text{Nd}_x\text{Y}_{3-x}\text{Fe}_5\text{O}_{12}$  nanoparticles are listed in Table 2, with an error of  $\pm 3.55$ – $6.83$  nm. The slightly larger values of the particle size obtained from the TEM images compared with that obtained from the XRD analysis may be due to the stretching of the grains caused by the magnetic interactions. The crystallinity index  $I_{\text{cry}} = D_{\text{TEM}}/D_{\text{XRD}}$  [32] was calculated and is listed in Table 2. The values of  $I_{\text{cry}}$  vary around 1, proving the high crystallinity of the prepared  $\text{Nd}_x\text{Y}_{3-x}\text{Fe}_5\text{O}_{12}$  nanoparticles, especially for  $0.5 < x < 1.5$ . Moreover, an obvious agglomeration of the  $\text{Nd}_x\text{Y}_{3-x}\text{Fe}_5\text{O}_{12}$  nanoparticles is observed as a result of the high surface energy and the permanent magnetic moment [33]. Because the system tends to minimize the total surface energy, attractive Van der Waals forces act upon and play a role in the agglomeration of the nanoparticles. Moreover, the magnetic forces created by the permanent magnetic moments of the  $\text{Fe}^{3+}$  ions give rise to magnetic interactions between the nanoparticles, proving the high reactivity of the composition [31]. The magnetic properties and dipolar moments of the nanoparticles play a key role in the agglomeration of the nanoparticles, especially in the absence of any surfactant [34]. Note that, it has been reported in the literature that particles having a diameter larger than 20 nm have enough magnetic moments that can overcome the Brownian motion of the particles [18]. Accordingly, the prepared nanoparticles do not suspend freely in the solvent and move randomly in a Brownian motion, but they agglomerate together under the effect of their magnetic interactions.

The nanoparticles morphology was confirmed by the SEM micrographs, presented in Fig. 5 for the prepared  $\text{Nd}_x\text{Y}_{3-x}\text{Fe}_5\text{O}_{12}$  nanoparticles, along with their corresponding EDX graphs, where agglomerated grains with irregular morphology appear in the SEM micrographs. The histograms of these micrographs were constructed and are displayed in Fig. 5. The grain size appears larger than the crystalline size evaluated in the XRD analysis. This is explained by the fact that in XRD analysis, the assessment is applied to the crystalline area in which the X-rays are diffracted in a coherent

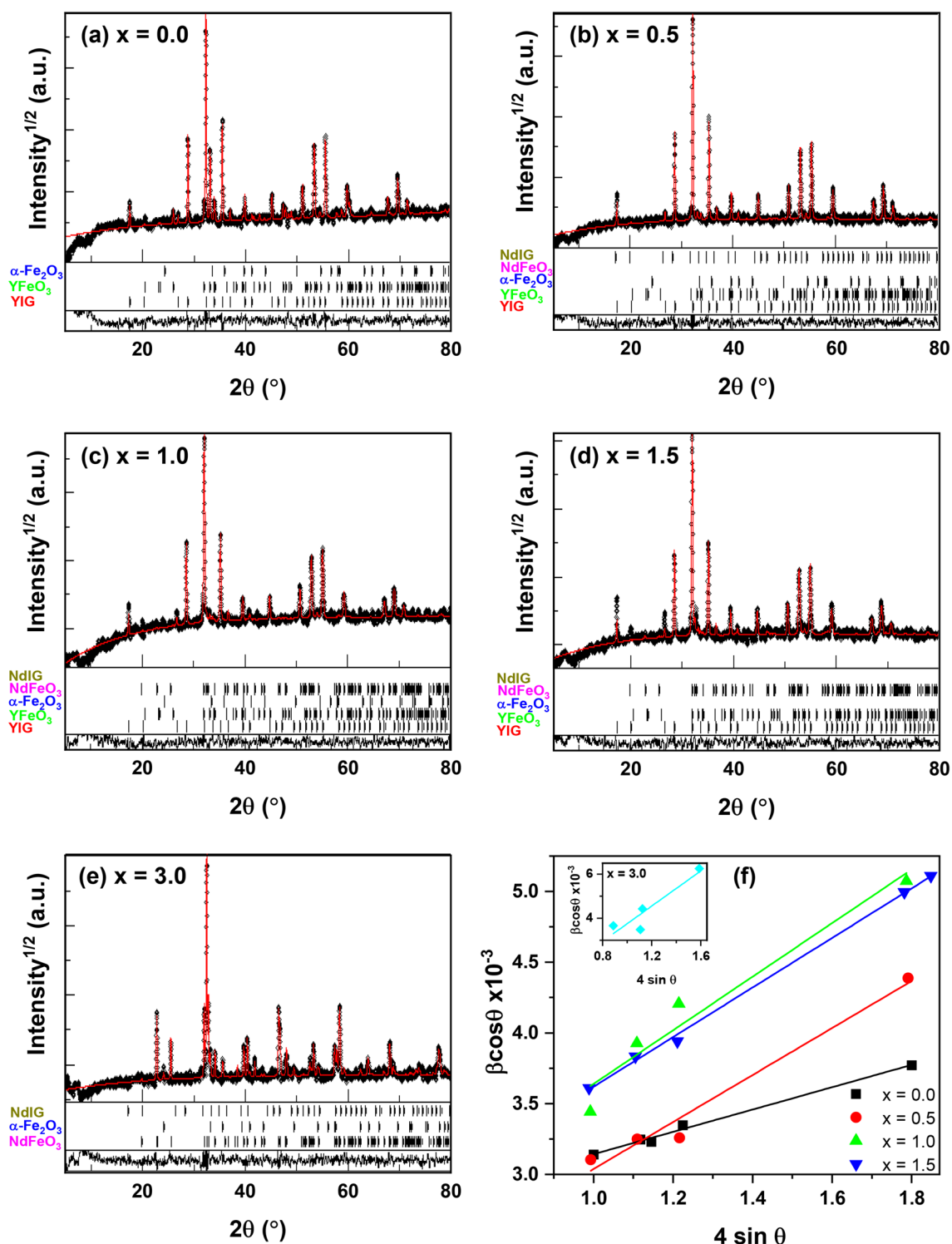


**Fig. 3** The phase contents of the synthesized nanoparticles with peak fitting as determined by the MAUD program and the W–H plots

manner; however, in SEM measurements the grain size is measured between the visible grain boundaries [35]. The Nd-doped samples exhibit a smaller grain size than the pure sample with a higher porous morphology, confirming the

porosity values listed in Table 2. This is due to the compression that occurred to the Garnet samples when doped with  $\text{Nd}^{3+}$  ions, causing deformation in the  $\text{Fe}^{2+}\text{-O}^{2-}\text{-Y}^{3+}$  and  $\text{Fe}^{2+}\text{-O}^{2-}\text{-Fe}^{3+}$  bond angles [31]. The analysis of the EDX

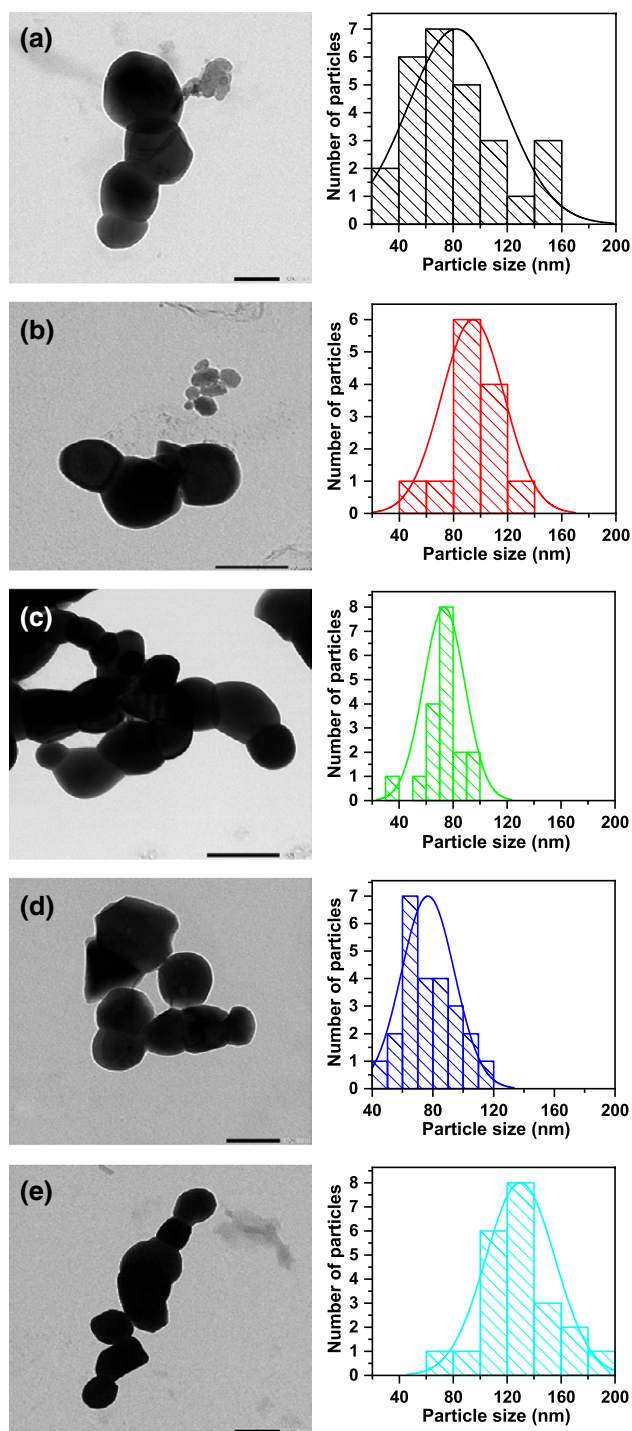


**Fig. 4** TEM images and histograms of  $\text{Nd}_x\text{Y}_{3-x}\text{Fe}_5\text{O}_{12}$  nanoparticles at different Nd-doping concentrations: **a**  $x=0.0$ , **b**  $x=0.5$ , **c**  $x=1.0$ , **d**  $x=1.5$  and **e**  $x=3.0$

data (Table 3) for all the samples shows that oxygen was the dominant element, followed by iron, yttrium, and neodymium, which is consistent with the proposed  $\text{Nd}_x\text{Y}_{3-x}\text{Fe}_5\text{O}_{12}$  formula. While no Nd was detected in pure YIG ( $x=0.0$ ), the atomic percentage of Nd in the  $\text{Nd}_x\text{Y}_{3-x}\text{Fe}_5\text{O}_{12}$  nanoparticles

( $x=0.5, 1.0, 1.5$ , and  $3.0$ ) increased as the level of doping increased, thus demonstrating the successful doping of Nd by the coprecipitation method, with no undesirable impurities.

### 3.4 Fourier-transform infrared (FTIR) spectroscopy

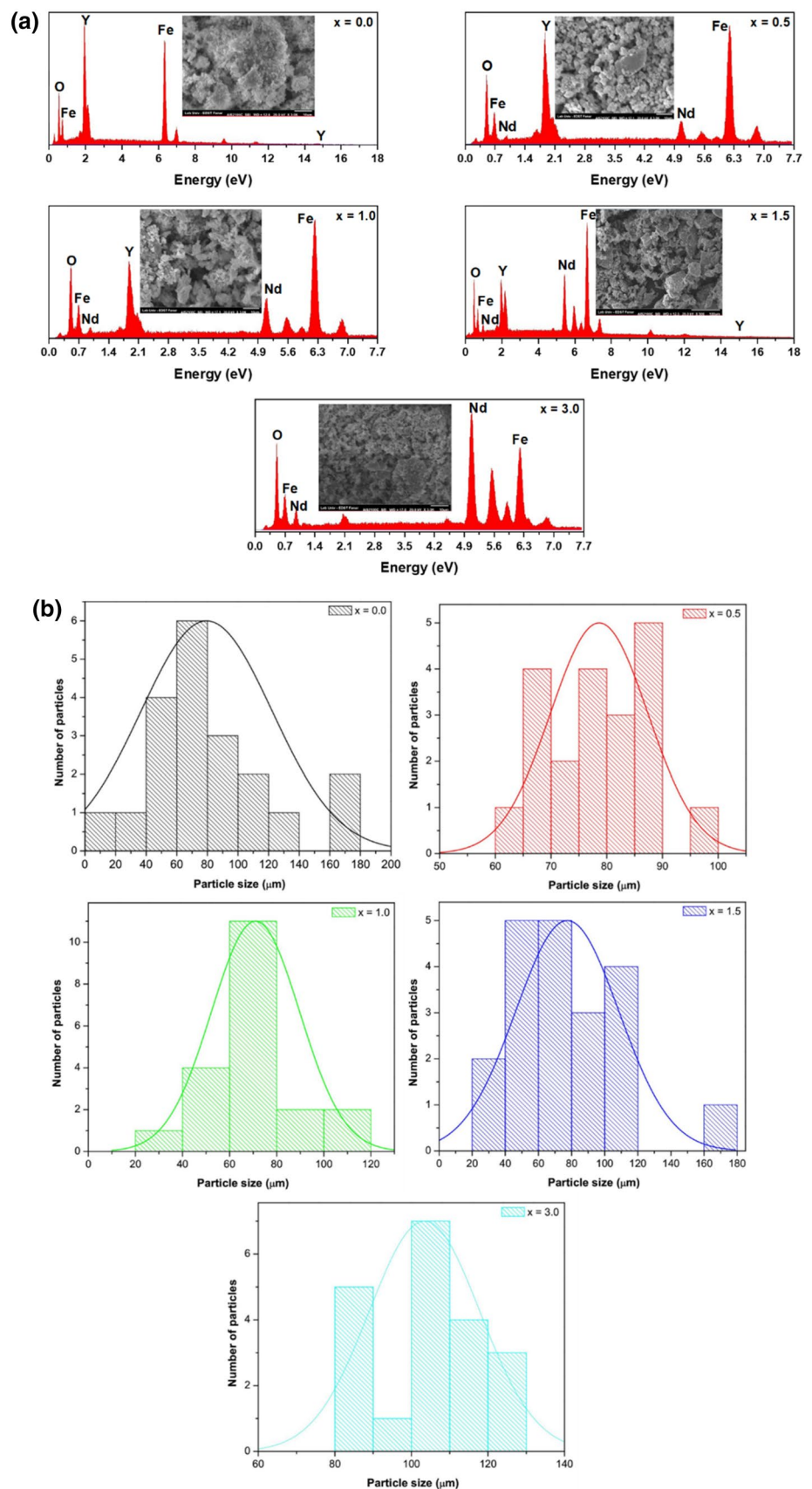
The successful synthesis of  $\text{Nd}_x\text{Y}_{3-x}\text{Fe}_5\text{O}_{12}$  nanoparticles was further confirmed by acquiring FTIR spectra as shown in Fig. 6. The three intense vibration bands at  $657.09$ ,  $600.58$ , and  $565.68\text{ cm}^{-1}$  are characteristic of the  $\text{FeO}_4$  tetrahedral in the YIG Garnet [9]. The absence of an absorption band at  $580\text{ cm}^{-1}$  contributing to the orthoferrite ( $\text{YFeO}_3$ ) further established the complete conversion of orthoferrite into YIG Garnet upon calcination at  $1050\text{ }^\circ\text{C}$ . Furthermore, a strong band at  $400\text{ cm}^{-1}$  was attributed to the isolated octahedral characteristic of YIG. The incorporation of the  $\text{Nd}^{3+}$  ions in the  $\text{Y}_3\text{Fe}_5\text{O}_{12}$  matrix shifted the absorption bands to the right.  $\text{Nd}^{3+}$  ion ( $1.12\text{ \AA}$ ) has a bigger ionic radius than  $\text{Y}^{3+}$  ions ( $1.02\text{ \AA}$ ). Therefore, the incorporation of  $\text{Nd}^{3+}$  ions into the dodecahedral site of YIG Garnet structure led to the distortion of the tetrahedron causing the observed shift in its characteristic bands. This was also associated with an increase in the lattice size as the degree of neodymium ion doping increased as revealed from the XRD data (Table 2). Besides, no significant changes can be seen in intensity and bands for the absorption bands for the doped samples ( $0.0 \leq x \leq 1.5$ ), where the characteristic band for Garnet formation continued to appear. On the other hand, the FTIR spectrum for  $x=3.0$  did not show the typical vibration modes of the Garnet structure, suggesting that the Garnet structure did not form. Instead, a strong band at  $553\text{ cm}^{-1}$  corresponding to Nd–O bonds of the  $\text{NdFeO}_3$  orthoferrite was observed, where an orthorhombic crystal structure can be proposed for this composition.

### 3.5 UV–Vis spectroscopy analysis

UV–Vis absorption analysis was performed to study the optical properties and to determine the energy bandgap of the prepared  $\text{Nd}_x\text{Y}_{3-x}\text{Fe}_5\text{O}_{12}$  nanoparticles. Figure 7a shows the UV–Vis absorption spectra of the prepared samples in the wavelength range  $250\text{--}700\text{ nm}$ . Rare earth metals (Nd and Y) are usually identified in the wavelength region of  $220\text{--}450\text{ nm}$  [36], whereas YIG ( $x=0.0$ ) showed a band maximum at  $358\text{ nm}$ ,  $\text{Nd}_{0.5}\text{Y}_{2.5}\text{Fe}_5\text{O}_{12}$ ,  $\text{Nd}_1\text{Y}_2\text{Fe}_5\text{O}_{12}$ , and  $\text{Nd}_{1.5}\text{Y}_{1.5}\text{Fe}_5\text{O}_{12}$  exhibited absorption maxima  $356$ ,  $351$ ,  $350\text{ nm}$ , respectively. The observed blue shift was attributed to the electronic transitions between the oxygen ions and the different cations in doped YIG nanoparticles [30].

Tauc's relation [37] calculated the optical bandgap ( $E_g$ ) of the prepared samples, and Tauc's plots of  $(\alpha h\nu)^n$  versus the photon energy  $h\nu$  are depicted in Fig. 7b, where  $\alpha$  is the

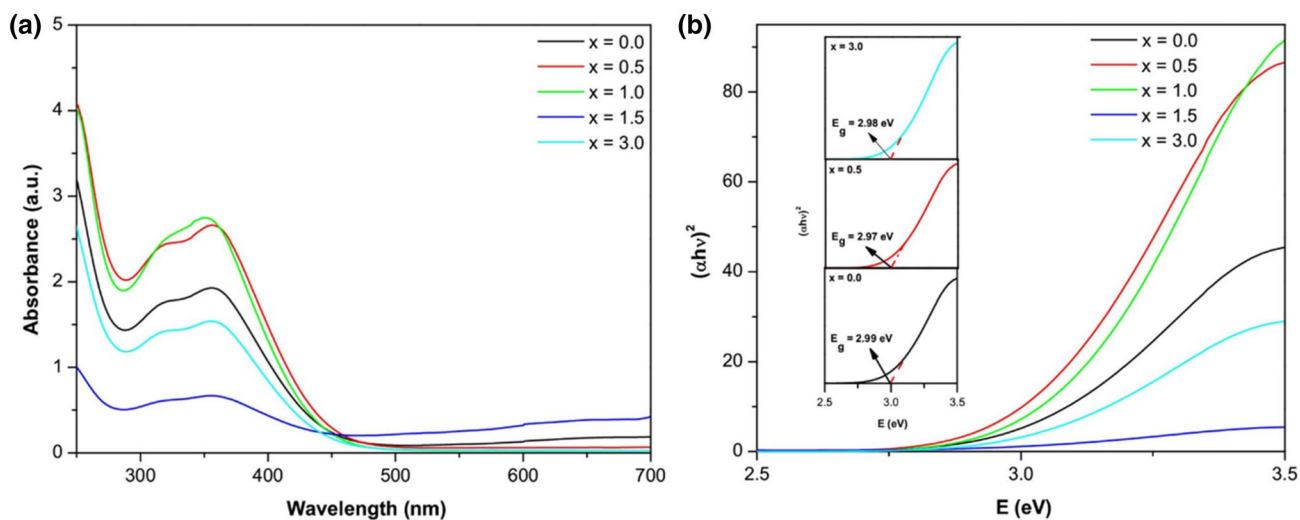
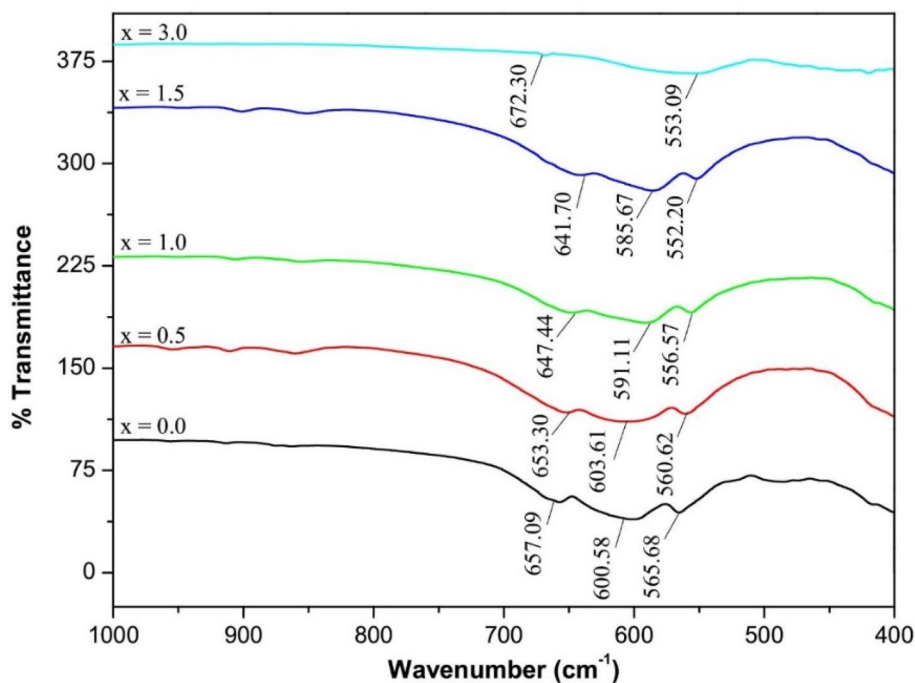
**Fig. 5** **a** EDX and SEM micrographs and **b** histograms of the SEM micrographs for  $\text{Nd}_x\text{Y}_{3-x}\text{Fe}_5\text{O}_{12}$  nanoparticles at different Nd-doping concentrations



**Table 3** Atomic percentage of the elemental composition in  $\text{Nd}_x\text{Y}_{3-x}\text{Fe}_5\text{O}_{12}$  nanoparticles

Element	Samples (at.%)				
	$x=0.0$	$x=0.5$	$x=1.0$	$x=1.5$	$x=3.0$
Y	14.26	14.69	11.60	10.40	–
Fe	21.26	25.02	25.53	30.40	23.16
O	39.42	46.49	47.78	40.58	47.88
Nd	–	2.88	5.48	11.45	21.08

absorption coefficient, while  $n$  takes on the values of 2 and 1/2 in case of allowed direct and allowed indirect optical transitions, respectively. No significant change in the band-gaps was observed at different Nd-doping levels, with calculated values ranging between 2.89 and 3.02 eV. These values are in agreement with literature reports [35] that showed  $E_g$  of 2.8 eV for YIG. The fact that  $E_g$  values fall in the range 2–4 eV suggested that the synthesized nanoparticles behaved as semiconductors.

**Fig. 6** FTIR spectra of  $\text{Nd}_x\text{Y}_{3-x}\text{Fe}_5\text{O}_{12}$  nanoparticles**Fig. 7** a UV-Vis spectra and b Tauc's plots of  $\text{Nd}_x\text{Y}_{3-x}\text{Fe}_5\text{O}_{12}$  nanoparticles

### 3.6 Photoluminescence properties of $\text{Nd}_x\text{Y}_{3-x}\text{Fe}_5\text{O}_{12}$ nanoparticles

Photoluminescence (PL) studies of  $\text{Nd}_x\text{Y}_{3-x}\text{Fe}_5\text{O}_{12}$  nanoparticles were conducted to gain insight into the effect of  $\text{Nd}^{3+}$  doping on the energies and of the excited states. PL spectra were acquired at room temperature upon excitation at 450 nm blue light under excitation-emission bandwidth of 5 nm, and emissions were recorded between 500 and 700 nm. Figure 8 shows the emission bands for the prepared samples sintered at 1050–1100 °C. Broad emission bands in the wavelength range 500–550 nm were obtained, and therefore, the green light was observed for all samples. The emission at 530 nm can be attributed to the  ${}^4\text{G}_{7/2} \rightarrow {}^4\text{I}_{9/2}$  transition [38, 39]. An increase in the PL intensity band (0.988 for  $x=0.0 \rightarrow 1.772$  for  $x=3.0$ ) was observed as  $\text{Nd}^{3+}$  content increased due to the additive contribution of  $\text{Nd}^{3+}$  ions towards the aforementioned transition. The peak at 530 nm in each curve ( $E=2.34$  eV) is ascribed to the near band edge emission (NBE) originated from the recombination of excitons (recombination of the electron with hole due to electrostatic Coulomb force). The detected peaks were in reasonable agreement with the bandgap energies obtained from UV–Vis spectroscopy [40]. The PL spectra were deconvoluted to Gaussian peaks as shown in Fig. 8a–e. All spectra revealed an intense peak at ~530 nm, showing the presence of green emissions that illustrate the existence of oxygen deficiencies in the samples since the green emissions originate from oxygen vacancies and singly ionized oxygen vacancies [41].

### 3.7 DC conductivity

The conductivity of the  $\text{Nd}_x\text{Y}_{3-x}\text{Fe}_5\text{O}_{12}$  nanoparticles was measured within a temperature range of 373.15–873.15 K, where all samples reached their maximum conduction at 873.15 K. Figure 9a shows that as the temperature increases, the conductivity of the samples increases, as a result of the increasing concentration of the charge carriers that can overcome the energy barrier to contribute in electrical conduction. The increase in conductivity can be attributed to point defects created by the doping process [35], and to an increase in charge carriers' hopping rate [42]. The obtained results corroborated the observations from UV–Vis spectroscopy, which showed that the samples are semiconductors as deduced from the energy gap measurements. Several factors can affect the point defects such as variation in atomic size between dopant and substituent, and the lattice site of host structure [35].

The DC conductivity temperature dependence was studied by the Arrhenius plot, illustrated in Fig. 9b. Two regions are revealed corresponding to two activation energies ( $E_{\text{aH}}$ ) and

( $E_{\text{aL}}$ ), related to the hopping process at high and low temperatures given by the Arrhenius equation [43]:

$$\sigma = \sigma_{\text{H}} \exp\left(-\frac{E_{\text{aH}}}{K_{\text{B}}T}\right) + \sigma_{\text{L}} \exp\left(-\frac{E_{\text{aL}}}{K_{\text{B}}T}\right) \quad (6)$$

where  $\sigma_{\text{H}}$  and  $\sigma_{\text{L}}$  are pre-exponential factors,  $K_{\text{B}}$  is the Boltzmann's constant, and  $T$  is the absolute temperature. Except for concentration  $x=3.0$ , the energy gap for all the prepared samples in the high-temperature region is higher than that in the low-temperature region (Table 4).

### 3.8 Magnetic properties of Nd-doped YIG nanoparticles

The magnetic hysteresis (M–H) loops of the prepared  $\text{Nd}_x\text{Y}_{3-x}\text{Fe}_5\text{O}_{12}$  nanoparticles, collected at room temperature, are depicted in Fig. 10. An obvious ferrimagnetic behavior is displayed by the Garnet samples ( $x < 3.0$ ), whereas a weak ferromagnetic behavior is exhibited by the orthoferrite sample ( $x=3.0$ ), as shown in the inset of Fig. 10. In the Garnet structure, the  $\text{Fe}^{3+}$  ions present in the octahedral (24d) sites couple antiferromagnetically with the  $\text{Fe}^{3+}$  ions in the tetrahedral [16a] sites, through  $\text{Fe}^{2+}-\text{O}^{2-}-\text{Fe}^{2+}$  superexchange interaction. As a result, a net ferromagnetic behavior arises due to the parallel alignment of the remaining uncoupled  $\text{Fe}^{3+}$  ions in the d-sites. Note that the presence of the non-magnetic  $\text{Y}^{3+}$  ions in the dodecahedral {24c} sites does not affect the net magnetization. Upon doping, the  $\text{Nd}^{3+}$  ions in the c-sites of the Garnet structure are arranged in ferromagnetic alignment with the existing uncoupled  $\text{Fe}^{3+}$  ions, thus enhancing the net magnetization [12]. On the other hand, the weak ferromagnetism in the orthoferrites is attributed to the Dzyaloshinskii–Moriya interaction between slightly canted  $\text{Fe}^{3+}$  ions [44]. In the distorted and slightly tilted orthorhombic unit cell, the spin moments of the  $\text{Fe}^{3+}$  ions are not perfectly antiparallel and are arranged non-collinearly, possessing a G-type spin structure, with the rare earth ions being disordered in a paramagnetic state, giving rise to a small net magnetization [45, 46]. Generally, the magnetic properties are affected by different extrinsic and intrinsic parameters, including particle size, morphology, material's composition, temperature, the technique of preparation, orbital and spin interactions of the metal ions at interstitial sites, cations movement, ferrimagnetic domains, internal structure and magnetocrystalline anisotropy [30, 47, 48].

The saturation magnetization ( $M_{\text{s}}$ ) of the obtained hysteresis loops was calculated using the law of approach to saturation, according to [40]:

$$M = M_{\text{s}} \left(1 - \frac{b}{H^2}\right) \quad (7)$$

where  $b$  is a factor related to anisotropy. Figure 11a–e shows the plot of  $M$  as a function of  $1/H^2$  at high field and its linear

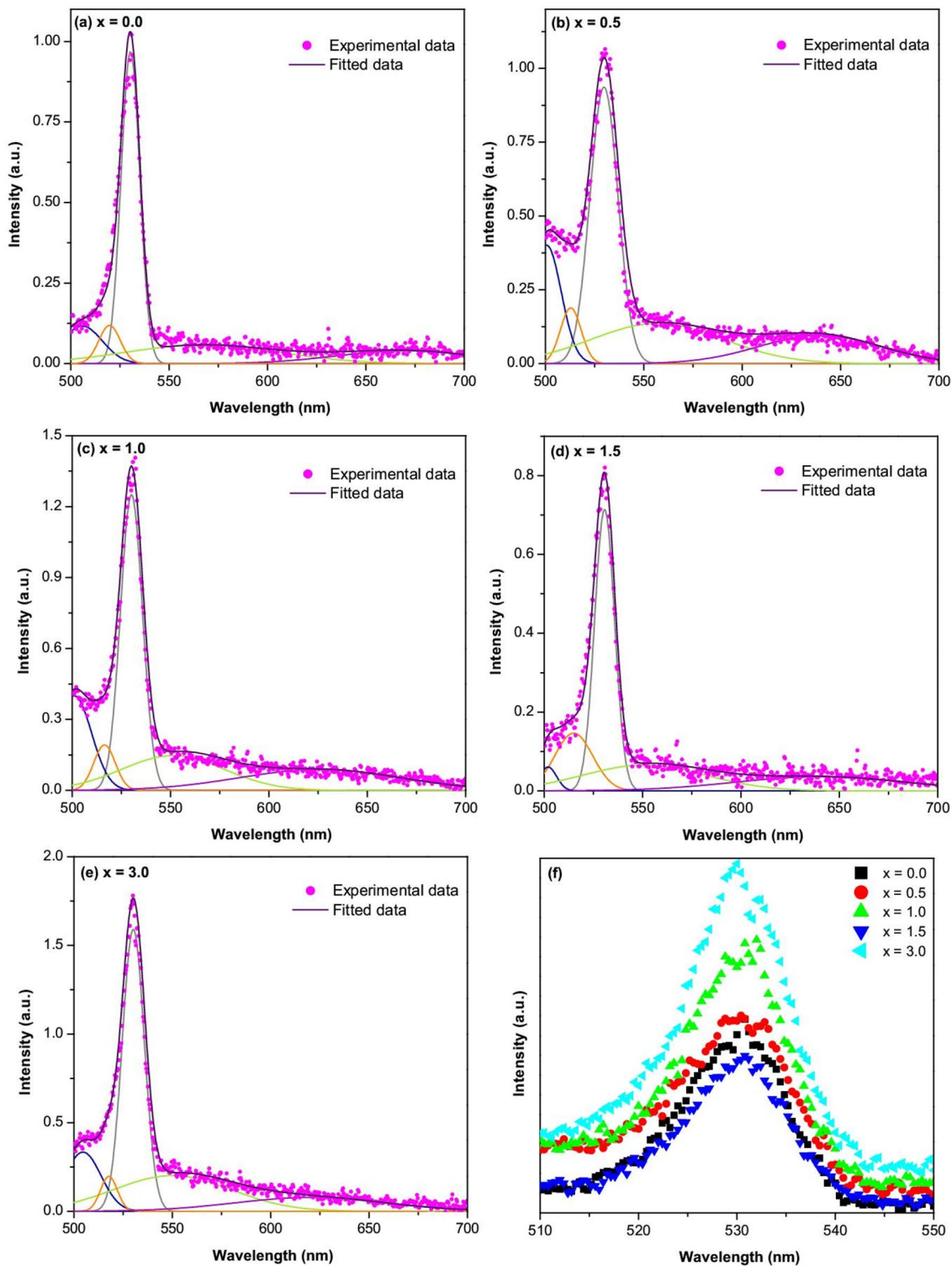


**Fig. 8** Deconvoluted PL spectra of  $\text{Nd}_x\text{Y}_{3-x}\text{Fe}_5\text{O}_{12}$  nanoparticles at different Nd-doping concentrations: **a**  $x=0.0$ , **b**  $x=0.5$ , **c**  $x=1.0$ , **d**  $x=1.5$  and **e**  $x=3.0$ , and **f** represents the PL spectra of all the samples in the wavelength range of 510–550 nm

fitting, from which the value of  $M_s$  was determined and is listed in Table 5. The value of  $M_s$  was found 18.658 emu/g for the pure YIG inconsistency with previous literature [49,

50]. Upon doping YIG by Nd,  $M_s$  increased and recorded a maximum value of 23.862 emu/g at the doping concentration of  $x=0.5$ , where the percentage of the Garnet phase

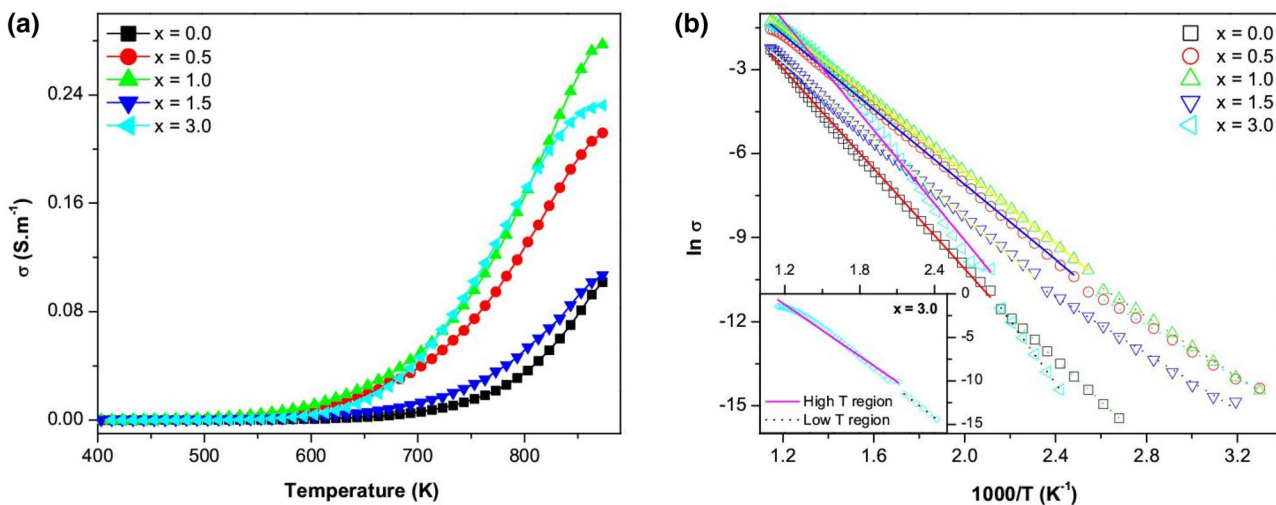


**Fig. 9** **a** The variation of the DC-electrical conductivity with temperature and **b** Arrhenius plot for  $\text{Nd}_x\text{Y}_{3-x}\text{Fe}_5\text{O}_{12}$  nanoparticles

**Table 4** Energy gaps and activation energies for  $\text{Nd}_x\text{Y}_{3-x}\text{Fe}_5\text{O}_{12}$  nanoparticles obtained from UV–Vis analysis and DC conductivity

$x$	$E_g$ (eV)	$E_{aH}$ (eV)	$E_{gL}$ (eV)
0.0	2.99	0.77	0.65
0.5	2.97	0.58	0.41
1.0	3.02	0.55	0.46
1.5	2.89	0.60	0.43
3.0	2.98	0.84	0.97

superexchange interaction. Moreover, the magnetic  $\text{Nd}^{3+}$  ( $3.62 \mu_B$ ) substitutes the non-magnetic  $\text{Y}^{3+}$  ( $0 \mu_B$ ), increasing the net magnetization of the sample [9]. It is noteworthy to point out that  $M_s$  increases as the crystallite size increases, as shown in Fig. 11f. On the other hand, the orthoferrite sample ( $x=3.0$ ) displays poor magnetic properties with  $M_s$  value equal to 0.828 emu/g, similar to previous studies [51, 52]. This highlights the weak ferromagnetic behavior, as a result of the formation of  $\text{NdFeO}_3$  (82.891%) and hematite (17.084%) [26]. The magnetic moment ( $n_B$ ) of the prepared samples was calculated according to [53]:

$$n_B = \frac{M \times M_s}{5585} \tag{8}$$

where  $M$  is the molecular weight of the samples. The presence of a higher  $n_B$  (Table 5) is noticed to give rise to higher values of  $M_s$ .

The remanent magnetization ( $M_r$ ) of the synthesized Garnets ranged between 0.10 and 4.24 emu/g. Pure YIG exhibited the highest  $M_r$  (4.24 emu/g), which is close to the value reported in the literature [30] for YIG (4.06 emu/g). Doping YIG by  $\text{Nd}^{3+}$  ions caused a decrease in the  $M_r$  values. The ratio of ( $M_r/M_s$ ), known as the squareness ratio, gives a significance concerning the uniaxial anisotropy contribution in  $\text{Nd}^{3+}$ -doped YIG generated by the internal strains [37]. The magnetic squareness values of the synthesized samples are less than 0.5 in the range of 0.078–0.227, indicating that the prepared samples have a multi-magnetic domain nature [53].

It has also been argued that the change in coercivity values of the doped YIG nanoparticles depends on the magnetic domain wall motion, as explained by the Stoner–Wohlfarth model [35, 54, 55]. It can be noticed that

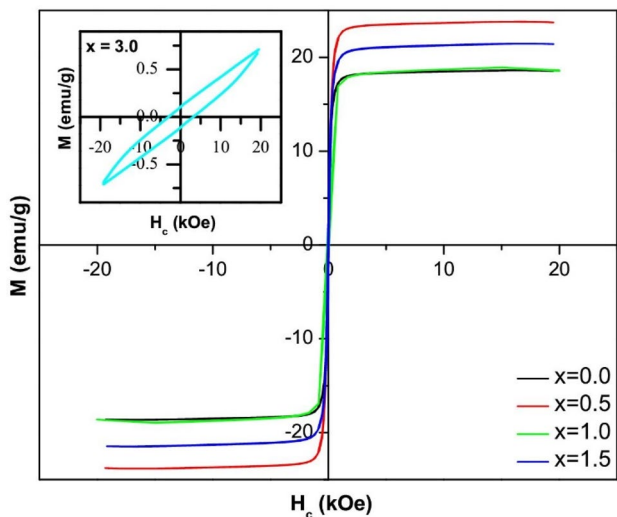


**Fig. 10** M-H loops for  $\text{Nd}_x\text{Y}_{3-x}\text{Fe}_5\text{O}_{12}$  nanoparticles at room temperature

present is the maximum. The higher values of  $M_s$  for the doped samples indicate that the  $\text{Nd}^{3+}$  ions at the c-site align with the uncoupled  $\text{Fe}^{3+}$  ions ferromagnetically by

**Fig. 11** Variation of  $M$  versus  $1/H^2$  curve of  $\text{Nd}_x\text{Y}_{3-x}\text{Fe}_5\text{O}_{12}$  nanoparticles for the different Nd-doping concentrations: **a**  $x=0.0$ , **b**  $x=0.5$ , **c**  $x=1.0$ , **d**  $x=1.5$  and **e**  $x=3.0$ , and **f** represents the variation of the obtained  $M_s$  as a function of the crystallite size  $D$

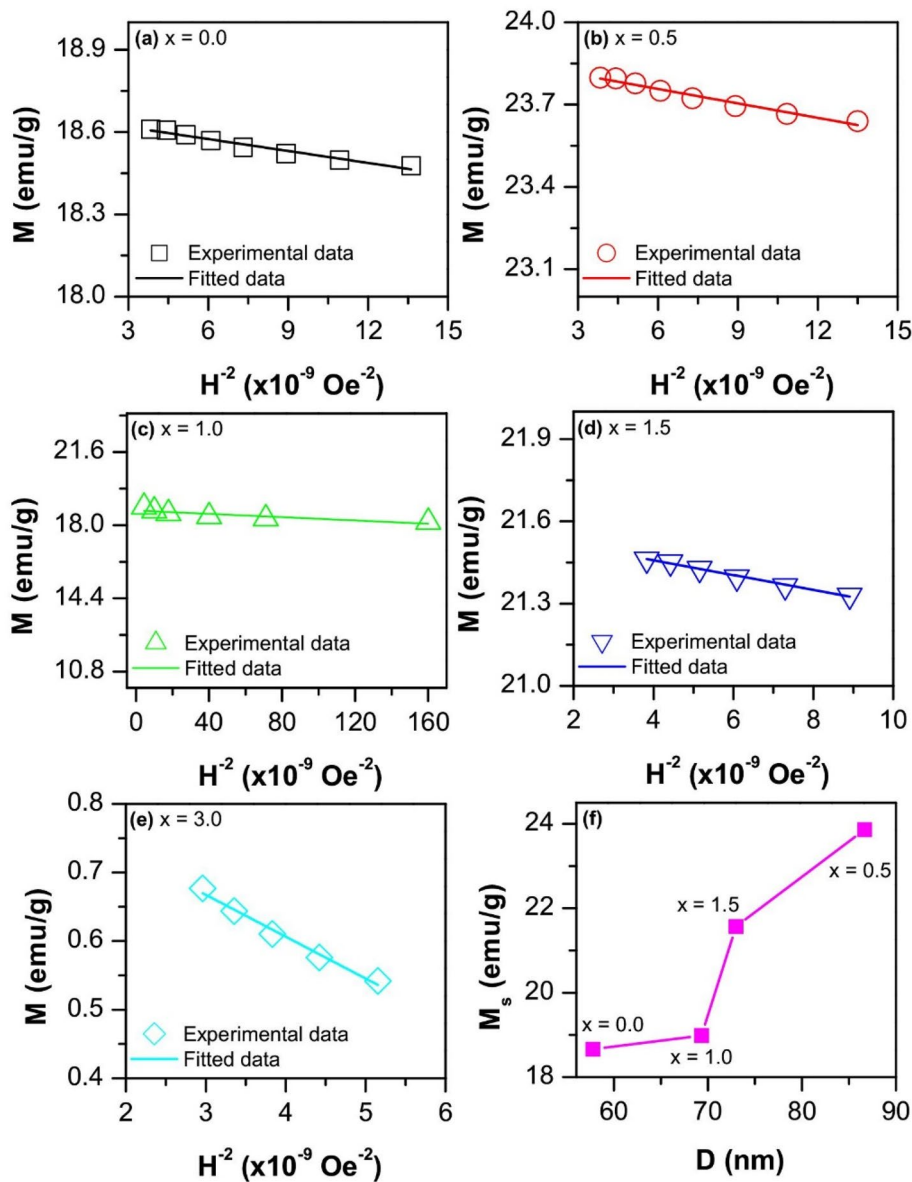


**Table 5** Magnetic parameters of  $\text{Nd}_x\text{Y}_{3-x}\text{Fe}_5\text{O}_{12}$  nanoparticles obtained from VSM results

$x$	$M_s$ (emu/g)	$M_r$ (emu/g)	$M_r/M_s$	$H_c$ (Oe)	$K$ (erg/g)	$n_B$ ( $\mu_B$ )	$N$	$\mu_i$
0.0	18.658	4.24	0.227	53.942	1048.39	2.469	1.754	19.18
0.5	23.862	1.87	0.078	21.757	540.79	3.275	0.325	91.24
1.0	18.987	1.98	0.104	87.149	1723.64	2.699	2.981	14.50
1.5	21.566	3.91	0.181	48.712	1094.29	3.172	1.297	31.02
3.0	0.828	0.10	0.120	3075.8	2652.88	0.134	2682.534	0.029

the coercivity  $H_c$  (Table 5) increases as the size increase for  $x=1.0$  and then decreases for the larger crystallite size for  $x=1.5$  and  $0.5$ . Furthermore, a prominent increase in  $H_c$  value occurred for  $x=3.0$  (3075.8 Oe), attributed to the existence of an orthoferrite phase that crystallizes in perovskite-type structure, and displays unique magnetic

properties such as a large  $H_c$  [56]. It should be noted that the coercivity of YIG and  $\text{Nd}^{3+}$ -doped YIG is larger than half the remanence magnetization, thus highlighting their potential use in high-frequency applications [22]. The variation in magnetic coercivity ( $H_c$ ) among the prepared samples can be attributed to the substitution of  $\text{Nd}^{3+}$  ions

that induce variations in Fe–O–Fe bond angle originating from the distortion of the oxygen polyhedrons. Such distortions in the Garnet structure influence the crystalline fields and magnetic anisotropy.  $H_c$  is related to the magnetocrystalline anisotropy  $K$  and  $M_s$  as inferred by the following relation [53]:

$$K = \frac{H_c \times M_s}{0.96} \quad (9)$$

Thus,  $K$  may be considered as the main factor for the  $H_c$  variation. The anisotropy constant  $K$  (Table 5) increases from 1048.39 erg/g for YIG to a maximum of 1723.64 erg/g for  $x = 1.0$ . Moreover, the Stoner–Wohlfarth model [57] describes the relationship between anisotropy constant and coercivity ( $H_c$ ) according to [30]:

$$H_c = \frac{2K}{M_s} - \frac{1}{2}(1 - 3N) \times M_s \quad (10)$$

where  $N$  is the demagnetization factor for the particles (Table 5). The initial permeability was determined using [58]:

$$\mu_i = M_s^2 \times \frac{D}{K} \quad (11)$$

## 4 Conclusion

Neodymium-doped yttrium iron Garnet,  $\text{Nd}_x\text{Y}_{3-x}\text{Fe}_5\text{O}_{12}$  ( $0.0 \leq x \leq 1.5$ ), and  $\text{NdFeO}_3$  ( $x = 3.0$ ) orthoferrite phase have been successfully prepared by the co-precipitation method at  $\text{pH} = 12$ , followed by annealing temperature in the range of 1050–1100 °C for 2 h. In this work, results showed that the rare earth metal Nd has a powerful influence on the structural, morphological, optical, electrical, and magnetic properties of YIG. The selection of the calcination temperatures was decided according to the thermal stability observed at ~810 °C from the TGA analysis. XRD confirmed the formation of the Garnet phase for  $0.0 \leq x < 3.0$ , and the orthoferrite phase was prominent for  $x = 3.0$ . The lattice constants ( $a$ ) were found to increase upon increasing  $\text{Nd}^{3+}$  concentrations. The formation of orthoferrite phases of Nd and Y was observed with the highest  $\text{Nd}^{3+}$  concentration. TEM and SEM revealed the presence of irregularly shaped nanoparticles with some agglomeration, and the elemental compositions were confirmed by EDX. The structural changes indicated from increasing  $\text{Nd}^{3+}$  ions were confirmed by FTIR analysis, in good agreement with the results obtained from XRD. The energy gaps obtained from Tauc's plots (2.89–3.02 eV) and the increasing DC conductivity trend as a function of temperature confirmed the semiconducting behavior of the prepared samples. PL

showed that the emission intensity is affected by increasing the concentration of  $\text{Nd}^{3+}$  ions. Nd-doped YIG samples showed ferrimagnetic behavior assigned to the inherent structure, while the orthoferrite ( $\text{NdFeO}_3$ ) phase showed a weak ferromagnetic behavior during magnetization measurements, which rely on the composition of the materials and their particle size.

**Acknowledgements** This work was performed in the Specialized Materials Science Laboratory, Physics Department, and Organic Chemistry Research Laboratory, Chemistry Department, Faculty of Science, Beirut Arab University. The authors would like to thank Ms. Alaa Abdallah from the Physics Department at BAU for assisting in data analysis, Dr. Rodaina Sayyed Hassan, and Dr. Salam Noureddine from the Lebanese University for conducting the XRD and SEM experiments, respectively, and Ms. Batoul Maatouk from AUB for conducting the TGA experiment.

**Funding** No specific funding was received for this work.

**Availability of data and materials (data transparency)** All data generated or analyzed during this study are included in this published article.

**Declaration**

**Conflict of interest** The authors declare that they have no known competing financial interests or personal relationships that could have appeared to influence the work reported in this paper.

## References

1. Y.Y. Kim, *Nanomaterials* (Basel) **7**, 207 (2017)
2. A. Paesano, S.C. Zanatta, S.N. De Medeiros, L.F. Cótica, J.B.M. Da Cunha, *Hyperfine Interact.* **161**, 211 (2005)
3. V. Sharma, J. Saha, S. Patnaik, B.K. Kuanr, *J. Magn. Magn. Mater.* **439**, 277 (2017)
4. B. Bhoi, N. Venkataramani, S. Prasad, R.P.R.C. Aiyar, G. Kumar, I. Samajdar, M. Kostylev, *J. Magn. Magn. Mater.* **483**, 191 (2019)
5. Y.R. Uhm, J.C. Lim, S.M. Choi, C.S. Kim, *J. Magn.* **21**, 303 (2016)
6. M. Niyafar, A. Beitollahi, N. Shiri, M. Mozaffari, J. Amighian, *J. Magn. Magn. Mater.* **322**, 777 (2010)
7. M.C. Onbasli, L. Beran, M. Zahradník, M. Kučera, R. Antoš, J. Mistrík, G.F. Dionne, M. Veis, C.A. Ross, *Sci. Rep.* **6**, 23640 (2016)
8. Z. Cheng, H. Yang, L. Yu, W. Xu, *J. Mater. Sci. Mater. Electron.* **19**, 442 (2008)
9. E. Baños-López, F. Sánchez-De Jesús, C.A. Cortés-Escobedo, A. Barba-Pingarrón, A.M. Bolarín-Miró, *Materials* **11**, 1652 (2018)
10. P.B.A. Fechine, E.N. Silva, A.S. de Menezes, J. Derov, J.W. Stewart, A.J. Drehman, I.F. Vasconcelos, A.P. Ayala, L.P. Cardoso, A.S.B. Sombra, *J. Phys. Chem. Solids* **70**, 202 (2009)
11. R.S. Azis, M.M. Syazwan, N.M.M. Shahrani, A.N. Hapishah, R. Nazlan, F.M. Idris, I. Ismail, M.M.M. Zulkimi, I.R. Ibrahim, Z. Abbas, N.M. Saidu, *J. Mater. Sci. Mater. Electron.* **29**, 8390 (2018)
12. E. Baños-López, C.A. Cortés-Escobedo, F. Sánchez-De Jesús, A. Barba-Pingarrón, A.M. Bolarín-Miró, *J. Alloys Compd.* **730**, 127 (2018)
13. V. Sharma, B.K. Kuanr, *J. Alloys Compd.* **748**, 591 (2018)

14. V. Sharma, J. Saha, S. Patnaik, B.K. Kuanr, *AIP Adv.* **7**, 056405 (2017)
15. O. Rosales-González, F. Sánchez De Jesús, F. Pedro-García, C.A. Cortés-Escobedo, M. Ramírez-Cardona, A.M. Bolarín-Miró, *Materials* **12**, 2054 (2019)
16. M. Mansournia, M. Orae, *J. Rare Earths* **36**, 1292 (2018)
17. J. Liu, Q. Jin, M. Yang, P. Yu, M. Ren, Y. Liu, L. Nong, Z. Kang, J. Lyu, X. Song, M. Zhang, *J. Electron. Mater.* **48**, 6661 (2019)
18. S. Hosseinzadeh, M. Behboudnia, L. Jamilpanah, M.H. Sheikhi, E. Mohajerani, K. Tian, A. Tiwari, P. Elahi, S.M. Mohseni, *J. Magn. Magn. Mater.* **476**, 355 (2019)
19. J. Liu, Q. Jin, S. Wang, P. Yu, C. Zhang, C. Luckhardt, Z. Su, R. Barua, V.G. Harris, *Mater. Chem. Phys.* **208**, 169 (2018)
20. X.Z. Guo, B.G. Ravi, P.S. Devi, J.C. Hanson, J. Margolies, R.J. Gambino, J.B. Parise, S. Sampath, *J. Magn. Magn. Mater.* **295**, 145 (2005)
21. M.A. Musa, R.S. Azis, N.H. Osman, J. Hassan, T. Zangina, *Results Phys.* **7**, 1135 (2017)
22. M.N. Akhtar, M. Yousaf, S.N. Khan, M.S. Nazir, M. Ahmad, M.A. Khan, *Ceram. Int.* **43**, 17032 (2017)
23. H.K. Jung, C.H. Kim, A.-R. Hong, S.H. Lee, T.C. Kim, H.S. Jang, D.H. Kim, *Ceram. Int.* **45**, 9846 (2019)
24. O. Opuchovic, A. Kareiva, K. Mazeika, D. Baltrunas, *J. Magn. Magn. Mater.* **422**, 425 (2017)
25. T. Arun, M. Vairavel, S. Gokul Raj, R. Justin Joseyphus, *Ceram. Int.* **38**, 2369 (2012)
26. M. Yousefi, S. Zeid, M. Khorasani-Motlagh, *Curr. Chem. Lett.* **6**, 23 (2017)
27. P. Bindu, S. Thomas, *J. Theor. Appl. Phys.* **8**, 123 (2014)
28. A. Monshi, M.R. Foroughi, M.R. Monshi, *World J. Nano Sci. Eng.* **02**, 154 (2012)
29. Y. Zhang, A. Sun, L. Shao, N. Suo, L. Yu, Z. Zuo, *Appl. Phys. A* **126**, 932 (2020)
30. M. Yousaf, A. Noor, S. Xu, M.N. Akhtar, B. Wang, *Ceram. Int.* **46**, 16524 (2020)
31. R.B. Borade, S.E. Shirsath, G. Vats, A.S. Gaikwad, S.M. Patange, S.B. Kadam, R.H. Kadam, A.B. Kadam, *Nanoscale Adv.* **1**, 403 (2019)
32. J. Al Boukhari, A. Khalaf, R. Awad, *J. Alloys Compd.* **820**, 153381 (2020)
33. M. Niyafar, H. Mohammadpour, N. Khalafi, *J. Alloys Compd.* **688**, 357 (2016)
34. S. Hosseynzadeh Khezri, A. Yazdani, R. Khordad, *Eur. Phys. J. Appl. Phys.* **59**, 30401 (2012)
35. F. Mohamed, F.A. Dar, S. Rubab, M. Hussain, L.-Y. Hua, *Ceram. Int.* **45**, 2418 (2019)
36. M. Martin, R.C. Martin, S. Allman, D. Brice, A. Wymore, N. Andre, *Spectrochim. Acta B. At. Spectrosc.* **114**, 65 (2015)
37. J. Al Boukhari, A. Khalaf, R. Sayed Hassan, R. Awad, *Appl. Phys. A* **126**, 323 (2020)
38. M. Shoab, G. Rooh, N. Chanthima, H.J. Kim, J. Kaewkhao, *Optik* **199**, 163218 (2019)
39. J.H. Kim, P.H. Holloway, *Appl. Phys. Lett.* **85**, 1689 (2004)
40. A.M. Abdallah, R. Awad, *J. Supercond. Nov. Magn.* **33**, 1395 (2020)
41. M. Almoussawi, A.M. Abdallah, K. Habanjar, R. Awad, *Mater. Res. Express* **7**, 105011 (2020)
42. J. Al Boukhari, A. Khalaf, R. Awad, *Appl. Phys. A* **126**, 74 (2020)
43. U. Godavarti, V.D. Mote, M. Dasari, *J. Asian Ceram. Soc.* **5**, 391 (2017)
44. A. Somvanshi, S. Husain, S. Manzoor, N. Zarrin, W. Khan, *J. Alloys Compd.* **806**, 1250 (2019)
45. K.P. Belov, A.M. Kadomtseva, *Sov. Phys. Usp.* **14**, 154 (1971)
46. K. Bouziane, A. Yousif, I.A. Abdel-Latif, K. Hricovini, C. Richter, *J. Appl. Phys.* **97**, 10A504 (2005)
47. D.S. Winatapura, A. Mulyawan, A.A. Wisnu, Yunasfi, *Key Eng. Mater.* **855**, 52 (2020)
48. N. Rodziah, M. Hashim, I.R. Idza, I. Ismayadi, A.N. Hapishah, M.A. Khamirul, *Appl. Surf. Sci.* **258**, 2679 (2012)
49. R. Nazlan, M. Hashim, I.R. Ibrahim, F. Mohd Idris, W.N. Wan Ab Rahman, N.H. Abdullah, I. Ismail, S. Kanagesan, Z. Abbas, R.S. Azis, *J. Mater. Sci. Mater. Electron.* **26**, 3596 (2015)
50. M.N. Akhtar, A. Bakar Sulong, M.A. Khan, M. Ahmad, G. Murtaza, M.R. Raza, R. Raza, M. Saleem, M. Kashif, *J. Magn. Magn. Mater.* **401**, 425 (2016)
51. P. Vera Serna, C. García Campos, F. Sánchez De Jesús, A. M. Bolarín Miró, J. A. Juanico Lorán, J. Longwell, P. Vera Serna, C. García Campos, F. Sánchez De Jesús, A. M. Bolarín Miró, J. A. Juanico Lorán, J. Longwell, *Mater. Res.* **19**, 389 (2016).
52. T.A. Nguyen, V. Pham, T.L. Pham, L.T.T. Nguyen, I.Y. Mittova, V.O. Mittova, L.N. Vo, B.T.T. Nguyen, V.X. Bui, E.L. Viryutina, *Curr. Comput. Aided Drug Des.* **10**, 219 (2020)
53. N. Raghuram, T.S. Rao, K.C.B. Naidu, *Appl. Phys. A* **125**, 839 (2019)
54. E.C. Stoner, E.P. Wohlfarth, *Philos. Trans. R. Soc. Lond. Ser. A Math. Phys. Sci.* **240**, 599 (1948)
55. D. Xue, W. Ma, *Electronics* **8**, 366 (2019)
56. L. Pan, X. Zhang, J. Wang, Q. Liu, *Ceram. Int.* **43**, 1236 (2017)
57. M.R. Khalifeh, H. Shokrollahi, S.M. Arab, H. Yang, *Mater. Chem. Phys.* **247**, 122838 (2020)
58. R. Nazlan, M. Hashim, I. Ismail, R.S. Azis, J. Hassan, Z. Abbas, F.M. Idris, I.R. Ibrahim, *J. Mater. Sci. Mater. Electron.* **28**, 3029 (2017)

**Publisher's Note** Springer Nature remains neutral with regard to jurisdictional claims in published maps and institutional affiliations.